Experimental and Computational Fluid Dynamic Study of Water Flow and Submerged Depth Effects on a Tidal Turbine Performance

Erfan Ghamati [1], Hamed Kariman [2] and Siamak Hoseinzadeh [3,*]

[1] Department of Mechanical and Energy Engineering, Shahid Beheshti University, Tehran 19839 69411, Iran
[2] School of Engineering, Edith Cowan University, 270 Joondalup Drive, Joondalup, WA 6027, Australia
[3] Department of Planning, Design, and Technology of Architecture, Sapienza University of Rome, 00185 Rome, Italy
* Correspondence: siamak.hosseinzadeh@uniroma1.it

Abstract: This study involves an experimental and numerical analysis of the Hunter turbine, a vertical axis turbine utilized for tidal energy. A laboratory model of the Hunter turbine, featuring an aspect ratio of 1.2, was designed and tested. Numerical equations, including the Reynolds-averaged Navier–Stokes (RANS) constant, were analyzed through computational fluid dynamics (CFD) software using the k-ω turbulence model to forecast turbine performance and other related flow specifications, such as pressure lines, stream velocity, and pressure. This simulation was conducted on the surface of the turbine blade, and the results were obtained accordingly. The experimental data were utilized to verify the numerical results, and the difference between the two was reasonably acceptable. The turbine was studied in six different flow coefficients and four different vertical positions. The results indicated that the power coefficient increased as the submerged depth from a water-free surface increased, and after a specific depth, the output power remained constant. It was also observed that the minimum depth from a water-free surface for maximum power coefficient was three times the diameter of the turbine drum (3D).

Keywords: computational fluid dynamic; tidal turbine; Hunter turbine; submerged depth effect; vertical axis turbine

1. Introduction

Climate change and energy security are two factors that have contributed to a global energy crisis. To address these issues, reducing fossil energy consumption and greenhouse gas emissions is one of the most critical factors. Rising energy efficiency and utilizing renewable energy (RE) sources, such as wind, solar, waves, and geothermal, can help decrease greenhouse gases [1,2]. One of the key ways to encourage industries to use REs is by determining environmental limits, such as greenhouse gases and global warming problems. Over the years, researchers have studied ocean waves, which are one of the most important sources of RE [3–5]. Compared to conventional energy sources, renewable energies are typically not economical. As a result, researchers and engineers are continuously designing low-cost machines with higher efficiencies and lower costs [5,6]. Hydro-kinetic conversion systems can be suitable for harnessing energy from tidal currents or artificially constructed water channels. Several studies have demonstrated that on-land water resources can be utilized for energy harvesting [6,7]. One of the advantages of tidal energy is that it can be produced by placing turbines in the path of waves [8,9]. Although typical maximum tidal currents are around 3 m/s, wind speeds may reach 12 m/s. Comparing dynamic pressures, they are still higher in water, which means that the dimensions of tidal turbines can be smaller than those of wind turbines for the same power output. The development of turbines, support structures, and cabling to land are the most critical factors for the development of tidal energy [10–13].

Tidal turbines can be classified into two types: horizontal axis tidal turbines (HATT) and vertical axis tidal turbines (VATT). So far, almost all tidal energy projects have primarily used HATT due to its advancements in wind energy technology. However, VATTs have various benefits for achieving tidal energy. Firstly, they operate independently of the flow direction. Secondly, their rotation speed is lower compared to HATTs, making them more efficient at low tidal speeds when the speed is less. Thirdly, they can be used better in shallow tidal currents because they can maximize the use of the available cross-sectional area [14,15]. However, VATTs also have some weaknesses, such as lower efficiency compared to HATTs and more difficulty in starting the work [15].

A new type of HATT is the Hunter turbine, which was invented by John Hunter to extract energy from a river or ocean stream [14]. The turbine consists of various flapping blades attached to a rotating drum. The turbine operates by opening the flapping blades when the impact flow hits the side of the drum, and the blades on the other side are allowed to flow by the current as long as they are controlled by the stops in the fully open situation.

Yang and Yawn conducted a study to investigate the performance of the Hunter turbine in a standalone type compared with fixed-blade turbines. They concluded that the optimal value of the flow coefficient was obtained in the range of 0.44 to 0.47, and the value of the optimal power coefficient in this range was equal to 0.19 by using a numerical simulation [16].

Chen et al. analyzed numerical simulations to analyze the impacts of a booster channel on the performance of VATT. They simulated the flow field with FLUENT software, used the finite volume method to solve the Reynolds-averaged Navier–Stokes equations and the SST k-ω turbulence model, and simulated the rotation of the rotor by solving the rotational motion equation. The results showed that for a single-channel turbine, the fluctuations of hydrodynamic torques and rotational speeds are significantly decreased, and the output power is 30% more than an independent turbine [17].

Sun et al. simulated the aerodynamic performance of a vertical tidal turbine with a suitable bionic super-hydrophobic surface on airfoils. They investigated the effect of different inlet velocities, the number of blades, and vertical tidal axis turbine solids with suitable bionic hydrophobic surfaces. The results showed that high energy efficiency could be enhanced by about 16.5% at the input speed U = 3 m/s. The increase in power factor is largely due to the blade number, input velocity, and strength at small tip ratios. However, the increase in energy efficiency could be independent of these aerodynamic factors at high tip ratios [18].

Jing et al. conducted various experiments on VATT and provided a wealth of experimental information to analyze the hydrodynamic function of turbines. They discussed the effect of different parameters on the hydrodynamic function of turbines and proposed control strategies for the blades of various turbines [19].

Derakhshan et al. conducted a numerical study on a horizontal axis tidal turbine (HATT) to investigate the impact of neighbor turbine distance, duct, and turbine layout on the power factor. The study found that the power factor increased for ducts with larger area ratios [20].

Maduka et al. performed flume tests on flanged duct turbines in tidal currents and found that these turbines produced 40% more power than bare turbines. However, accurate economic estimates for these turbines are not currently available [21].

De Arcos et al. used computational fluid dynamics (CFD) software to simulate the hydrodynamic effects of isolated flapping and torsional deformations on tidal turbine blades. The study showed that a pressure drop on the suction side of the blade increases the internal load [22].

Moreau et al. analyzed the environmental conditions and the effect of waves on the operation of vertical axis tidal turbines (VATTs) in France. The study analyzed the number of loads, frequency, and speed of waves on this type of turbine and found that VATTs are suitable for electricity generation in these areas [23].

Sun et al. used CFD software to investigate the effects of the number of blades on the performance of VATTs. The study showed that increasing the number of blades leads to a more homogeneous flow field and can improve efficiency at the start of operation [24].

Ma et al. investigated the hydrodynamic performance of a moving-state VATT and found that the twin-rotor in these systems can increase the power output efficiency. The study also found that the frequency and amplitude of the waves have less effect on the average output power of the turbine [25].

Satrio and Utama tested a VATT in Indonesia and presented a modified example of a VATT that has inclined vanes. The study found that this modified system has a better self-starting capability, making it work better in low tidal flow mode [26]. Chen et al. investigated and simulated the spatial evolution mechanism of a tidal current turbine experimentally. They concluded after this simulation that the kinetic energy in the wake region improves significantly in the range x = (2D, 3D) [27].

Xie et al. designed an innovative water turbine whose blades automatically open and close under the force of ocean currents, absorbing energy from various directions. The blades were shaped like a fish based on fluid dynamics principles, resulting in increased efficiency in electricity generation [28].

Han et al. investigated the macroscopic characteristics of tidal turbines and optimized their energy production farms using OpenTidalFarm software. The study concluded that adding more turbines to the set enhances power generation by 50% [29].

Manolesos et al. explored the application of vortex generators (VGs) to improve the performance of tidal turbines. The research results showed that VGs shorter than the local boundary layer can enhance blade profile performance and successfully reduce flow separation [30].

Wang et al. conducted an analysis and simulation of a new method to test the performance of a 300 W counter-rotating horizontal axis tidal turbine (HATT) using computational fluid dynamics (CFD). The findings were consistent between CFD predictions and laboratory data, and the turbine performed optimally at a blade tip speed ratio of 6–10 [31]. Samadi et al. investigated a hybrid turbine consisting of a new turbine with semi-cylindrical deflectors and a Savino's turbine in the Qeshm channel between the Persian Gulf and the Oman Sea to extract energy from a low-speed tidal current. Fluid dynamic analysis revealed that combining the proposed system with Savion's system increased power from 0.38 to 0.68 [32].

Khanjanpour and Javadi utilized the Taguchi technique to simulate vertical axis tidal turbines (VAT). Their analysis showed that the torsion angle is the most crucial factor affecting the hydrodynamic efficiency of the turbine, while the ratio of the chord to radius had the least impact [33].

Yang and Lavin studied four different designs of Hunter turbines with different ratios using numerical simulation. They concluded that 3D models produced significantly different results from 2D models and that 3D effects cannot be ignored for accurate turbine performance calculations. As the aspect ratio increases, the hydrodynamic parameters of the turbine become more uniform along the entire span, and with higher flow coefficients, the four designs exhibit similar performances and approach two-dimensional calculations [34]. Current turbines are usually installed over water streams and are exposed to various waves; different investigations have studied the performance of a floating structure [35–37].

According to predictions, a significant number of tidal turbines will be installed at a certain height above the water surface to allow for easy maintenance and repair of the system. Most turbines currently available are primarily designed for shallow water currents. However, when considering the installation of a turbine in a shallow river, placing it directly in the riverbed can lead to potential damage from debris carried by the flowing water. Thus, the optimal solution lies in installing the turbine at a specific elevation above the water surface. The objective of this research study is to investigate the impact of the turbine's height above the water surface on its performance. By studying the relationship between turbine height and performance, researchers can identify the optimal height that maximizes

the turbine's efficiency. Furthermore, understanding the effect of turbine height can help prevent potential damage caused by debris or other materials carried by the water. By determining the appropriate elevation, engineers can minimize the risk of turbine damage and prolong its operational lifespan. In this study, a Hunter turbine with six movable blades hinged on a revolving drum was manufactured and tested in a laboratory. The researchers studied the effect of the turbine's submerged depth on its performance. During experiments, the turbine was submerged at four different depths, namely 1D, 2D, 3D, and 4D (where D represents the diameter of the turbine). These depths represent the distance between the upper surface of the turbine and the water surface.

2. Methodology

To provide a detailed description of the Hunter turbine, Figure 1 highlights important factors. *R* in Figure 1 denotes the blade drum's diameter, and R_c represents the distance between the center of the blade chord and the blade drum when the blades are opened or closed. Additionally, Rt is the distance between the drum shaft and the fully open turbine blade. The angle of rotation is denoted by θ in this system, and θ1 is the angle between the flow and the drum to the center of the blade.
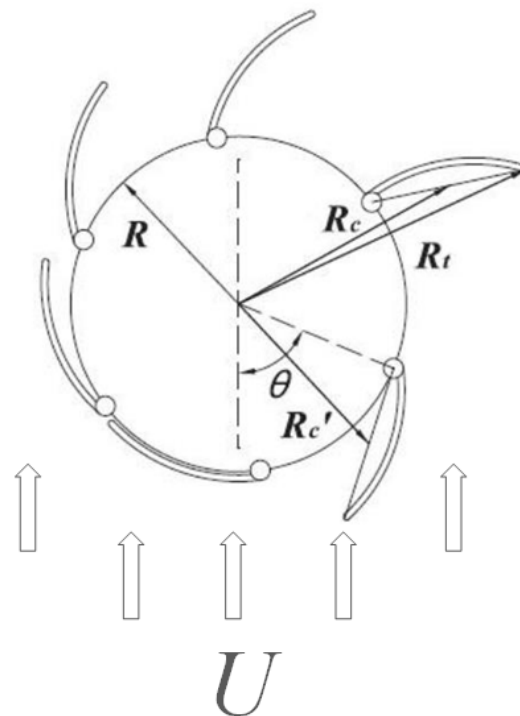

Figure 1. The definition of parameters.

To demonstrate the turbine's function, two dimensionless parameters are defined. The flow coefficient is calculated using Equation (1):

$$C_f = \frac{\omega R_c}{U} \tag{1}$$

In Equation (2), the power coefficient (C_p) is defined as the ratio of the actual power output (*P*) of the turbine to the power available in the incoming water flow ($\frac{1}{2}\rho A U^3$). The parameters *A*, *ρ*, *U*, and *T* represent the cross-sectional area of the turbine, water density, the velocity of the incoming flow, and the produced torque on the turbine, respectively.

$$C_p = \frac{P}{1/2\rho A U^3} = \frac{T \times \omega}{1/2\rho A U^3} \tag{2}$$

In the numerical simulation, by knowing U and ω and by solving the Reynolds-averaged Navier–Stokes equations with Ansys CFX software to find T, C_p can be calculated. However, in the experimental test, the water in the testing tunnel is motionless, the barge that holds the turbine moves with a specific speed, and the produced torque on the turbine is driven from the digital setup installed on the turbine.

Figure 2 illustrate the design parameters of the Hunter turbine and the blade positions at various angles. It should be noted that angle θ represents the angle between the flow direction and the end of the nearest blade to it.
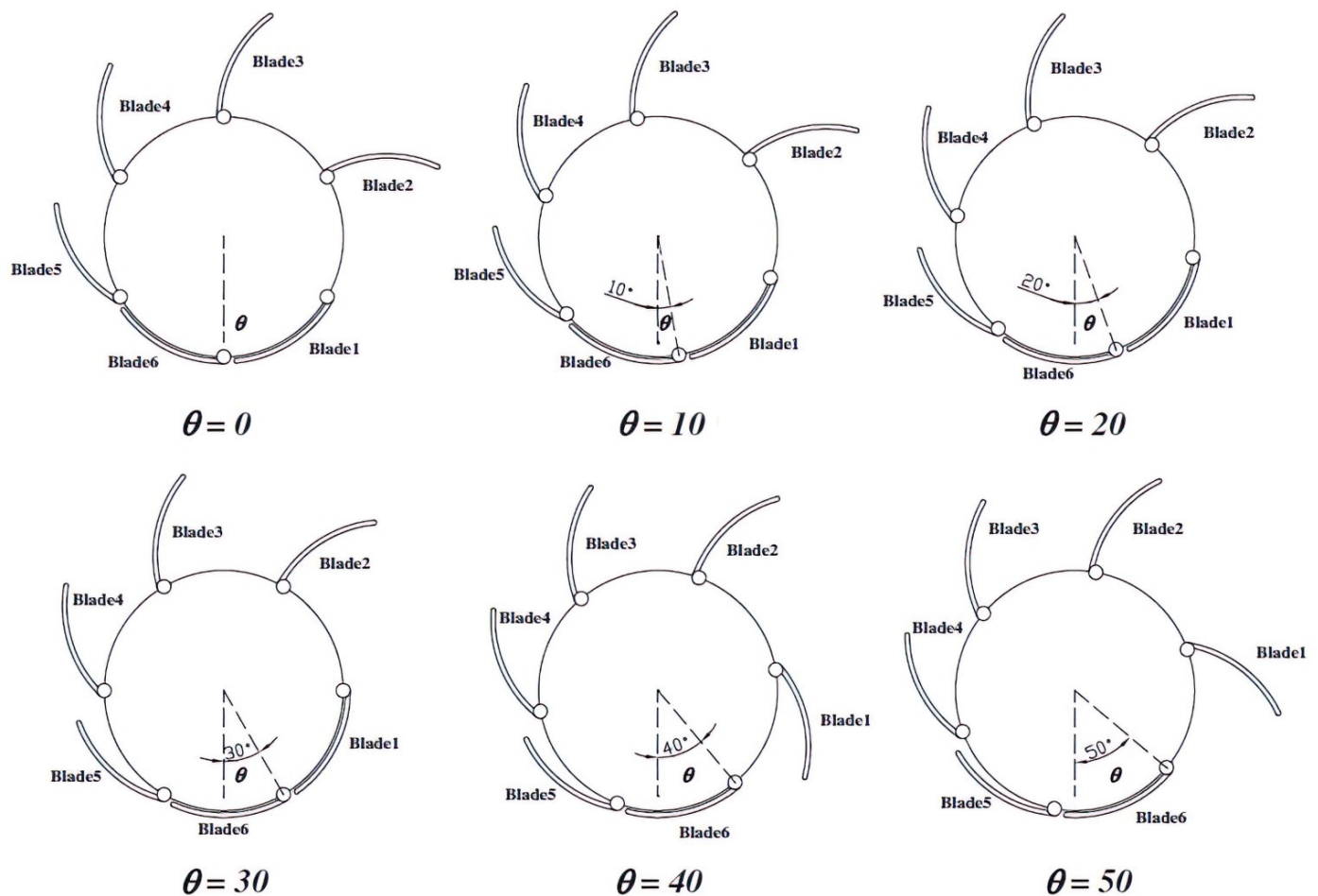
Figure 2. The position of blades at different angles.

3. Setup

The turbine assembly is composed of various components, such as a lengthy main shaft, a cylindrical body, and six blades. Figure 3 depicts that the turbine has a diameter of 100 mm, a height of 120 mm, and an aspect ratio (H/D) of 1.2. The testing channel used for experiments had a length of 500 m and a depth of 4.5 m, as illustrated in Figure 3.

(a)   (b)

Figure 3. Turbine laboratory (**a**), Test setup (**b**).

4. Numerical Setup

The ANSYS CFX software used in this study is a completely implicit flow solver based on the RANS solver method. This solver allows for a simultaneous solution of the equations of motion and continuity, resulting in a more accurate and efficient solution. Additionally, it eliminates the need for a pressure correction term to maintain mass conservation, which is beneficial in simulating boundary layer flows typically found in vertical axis turbines.

The k-ω turbulence model was chosen for this study to analyze the Reynolds stresses in the RANS equations because the discretization method for solving the problem was first order upwind. Yang proved that the k-ω model is suitable for a flow field simulation with a high angle of attack. Therefore, the k- ω turbulence model was selected to estimate the Reynolds stresses of the RANS equations. In addition, the k-ω turbulence model is known for its ability to provide accurate predictions of turbulent flow phenomena. It is particularly effective in capturing turbulent boundary layers; furthermore, the k-ω model excels at modeling near-wall flows, which is crucial in applications, such as turbine design. Furthermore, compared to more advanced turbulence models, such as Large Eddy Simulation (LES) and Direct Numerical Simulation (DNS), the k-ω model offers a good balance between accuracy and computational efficiency [38].

The turbine was designed using SolidWorks software and tested at six different rotation angles: 0, 10, 20, 30, 40, and 50 degrees. The blade positions at each angle were determined based on experimental tests conducted by Yang and Yawn. The computational domain of the turbine is illustrated in Figure 4.

The boundary condition for the computational domain (Figure 4) for the left, right, and lower surface is Wall. For the inlet and outlet, the boundary condition is Normal Speed and Average Relative Static Pressure: 0 Pa, relatively. The boundary condition of the upper surface is Opening.

In order to simulate the flow around the Hunter turbine, it was essential to generate appropriate grids for the computational domain. Both structured and unstructured grids were tested, but due to the complex geometry of the turbine and its curvature, especially during the closing, creating a structured grid proved to be complicated and difficult. Therefore, unstructured grids with tetrahedral cells were used to discretize the computational domain. The number of cells on the blades and the body of the turbine is illustrated in Figures 5 and 6, respectively.
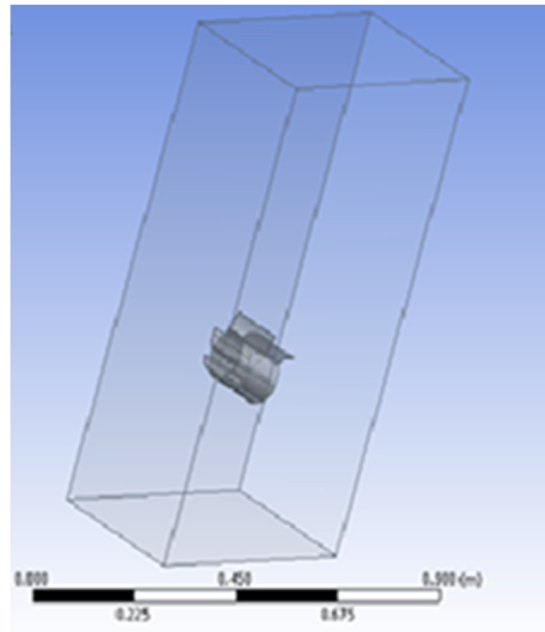
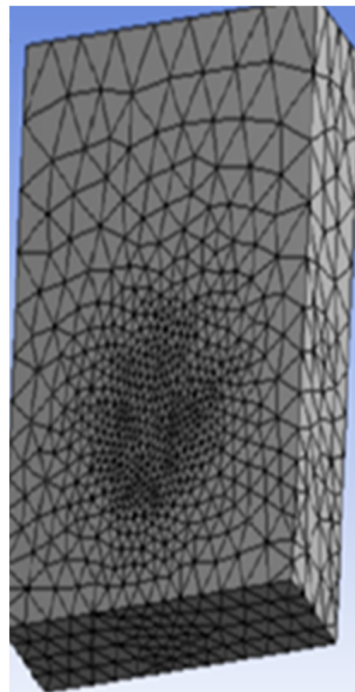**Figure 4.** The computational domain of the turbine.

Figure 5. Grids in the computational domain.

To ensure that simulation results are independent of mesh numbers, a mesh convergence test was performed at θ = 0, and the torque results as a function of grid number are presented in Figure 7. It can be observed that for more than 1,400,000 grids, the resulting answer becomes almost uniform, indicating that the simulation results are consistent and not significantly influenced by the mesh size.
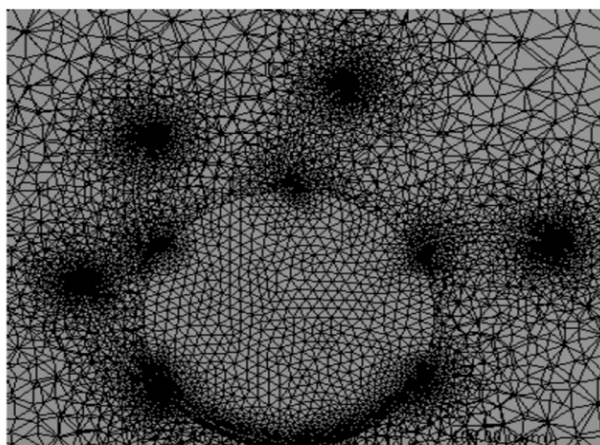
Figure 6. The number of cells on the blades and the body of the turbine.
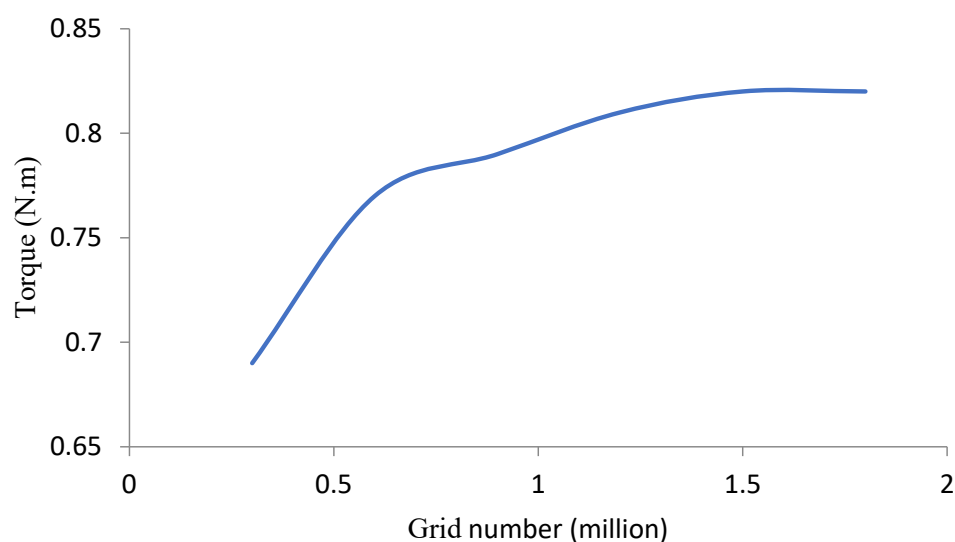
Figure 7. Grid independency.

5. Results and Discussion

5.1. The Performance of a Stand-Alone Turbine

To ensure the validity of the simulation results, a comparison was made between the numerical simulation data and experimental test results. The turbine was tested at six different flow velocities of 0.4 m/s, 0.7 m/s, 0.8 m/s, 1 m/s, 1.2 m/s, and 1.4 m/s, and the turbine was submerged to a depth of 2D. The flow coefficients corresponding to each of the six inlet velocities were 0.25, 0.32, 0.40, 0.46, 0.49, and 0.52.

The comparison of the overall performance between the experiments and the numerical simulation for a submerged depth of 2D is shown in Figure 8. Both experimental and numerical results show that the turbine power coefficient first increases with increasing flow coefficient, reaching a maximum value of C_p, and then decreases. The power coefficient obtained from the numerical solution for a flow coefficient of 0.47 was 0.185, while the experimental data yielded a power coefficient of 0.177. The turbine reaches its maximum performance at a flow coefficient of 0.47 for a submerged depth of 2D. The comparison of generated power by changing the flow velocity for the experimental test and the numerical simulation is presented in Table 1, which shows a small difference between the experimental and simulation results. The difference between the experimental and numerical simulations is because of two main factors: 1. experimental errors; 2. assumptions and boundary conditions in the computational domain.
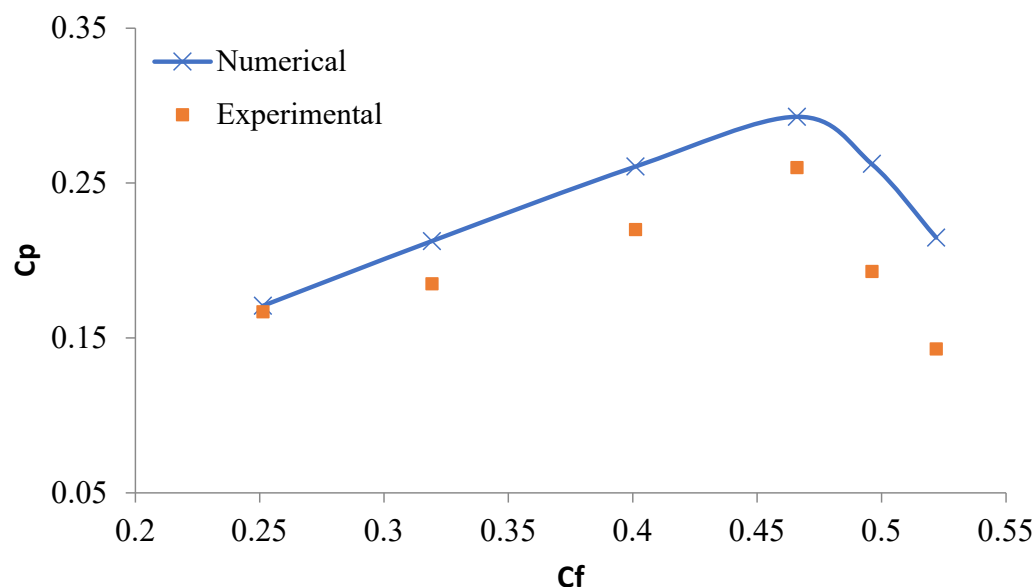
Figure 8. Comparison between calculated and experimental amounts of power coefficient.

Table 1. Comparison of experimental and numerical generated power.

Velocity (m/s)	Power (w)—Exp.	Power (w)—Nu.
0.4	0.017	0.09
0.7	0.11	0.17
0.8	0.19	0.29
1	0.44	0.53
1.2	0.58	0.78
1.4	0.89	1.06

The velocity contours and pressure contours at different angles and coefficients are displayed in Figures 9 and 10, respectively.

As depicted in Figure 10, the pressure on Blade 2 is considerably higher at $\theta = 0$ and $\theta = 50$, and it increases with the flow coefficient. However, at $\theta = 20$, there is no significant pressure difference on either side of Blade 2. The pressure difference across Blade 2 is utilized to generate torque, which causes the blade to rotate around the hinge pin when it is enlarged. The generated torque is observed to be greater at rotation angles of 0 and 50 compared to 20. At $\theta = 0$, blades 3, 4, and 5 are almost entirely closed and contribute little to the output torque, while only Blade 2 is fully opened and contributes significantly to the torque. Similarly, at $\theta = 50$, most of the output torque is produced by Blade 1, which is fully opened at this position. Additionally, raising the flow coefficient increases the pressure difference between the two blade surfaces, as shown in Figures 9 and 10 [13].

5.2. Effect of Turbine Submerged Depth on Its Performance

In this step, the performance of the Hunter turbine was evaluated at different submerged depths to determine the optimal vertical position for achieving the highest performance. Six flow velocities were tested, with corresponding flow coefficients of 0.25, 0.32, 0.40, 0.46, 0.49, and 0.52. The results, shown in Figure 11, indicate that as the flow coefficient increases, the turbine power coefficient initially increases and then decreases after reaching the maximum value of Cp. Additionally, as the vertical distance from the water surface increases, the turbine performance also increases, but only up to a certain height. Beyond this height, the power that can be obtained from the stream remains constant, and this height represents the optimal position for placing the turbine. The results indicate that the best position is at a depth of 3D, where the maximum power coefficient achieved by the turbine is 0.218 at a flow coefficient of 0.49.
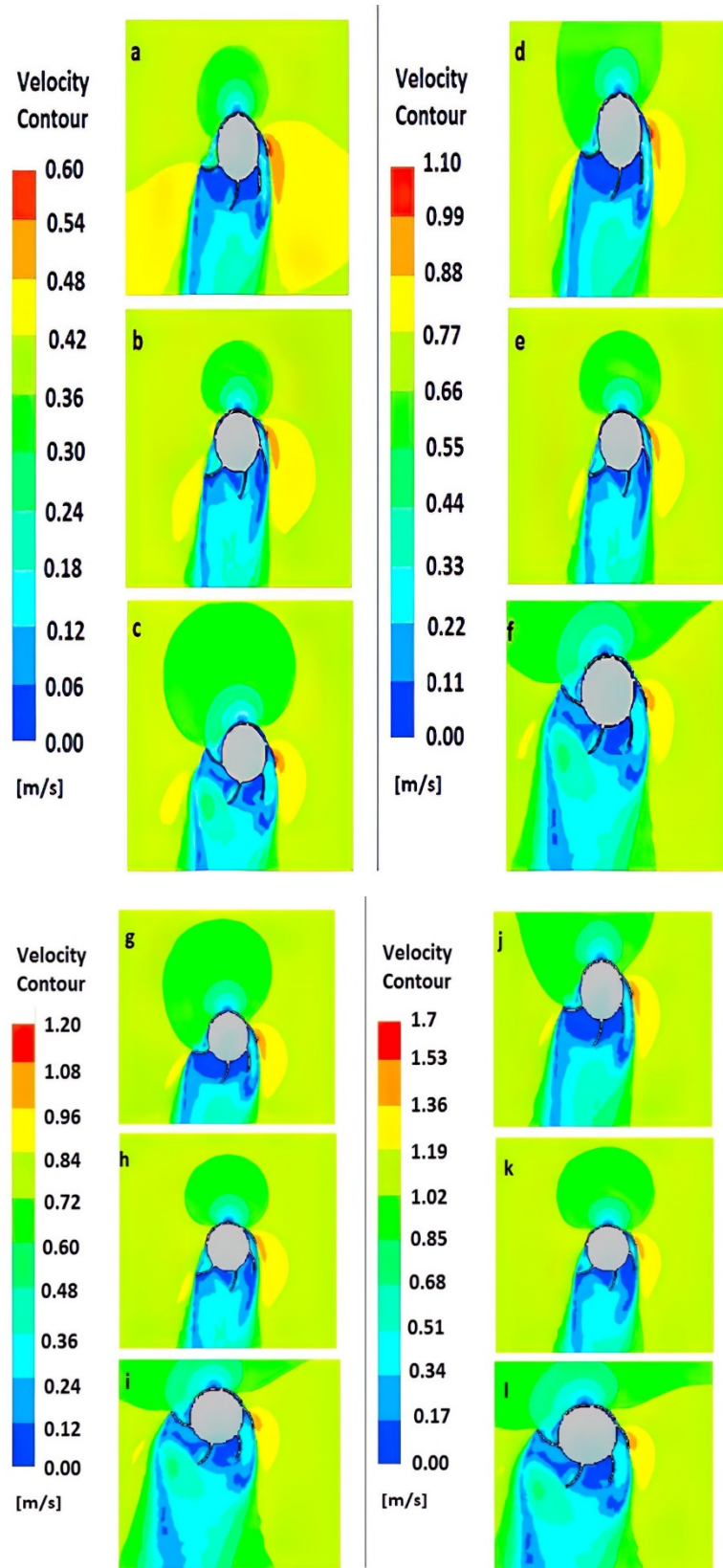
Figure 9. Velocity contours for 3D from θ = 0, 20, 50 and Cf 0.4 and 0.46. ((**a**): θ = 0, Cf = 0.4; (**b**): θ = 20, Cf = 0.4; (**c**): θ = 50, Cf = 0.4; (**d**): θ = 0, Cf = 0.46; (**e**): θ = 20, Cf = 0.46; (**f**): θ = 50, Cf = 0.46). θ = 0, 20, 50 and Cf 0.49 and 0.52. ((**g**): θ = 0, Cf = 0.49; (**h**): θ = 20, Cf = 0.49; (**i**): θ = 50, Cf = 0.49; (**j**): θ = 0, Cf = 0.52; (**k**): θ = 20, Cf = 0.52; (**l**): θ = 50, Cf = 0.52).
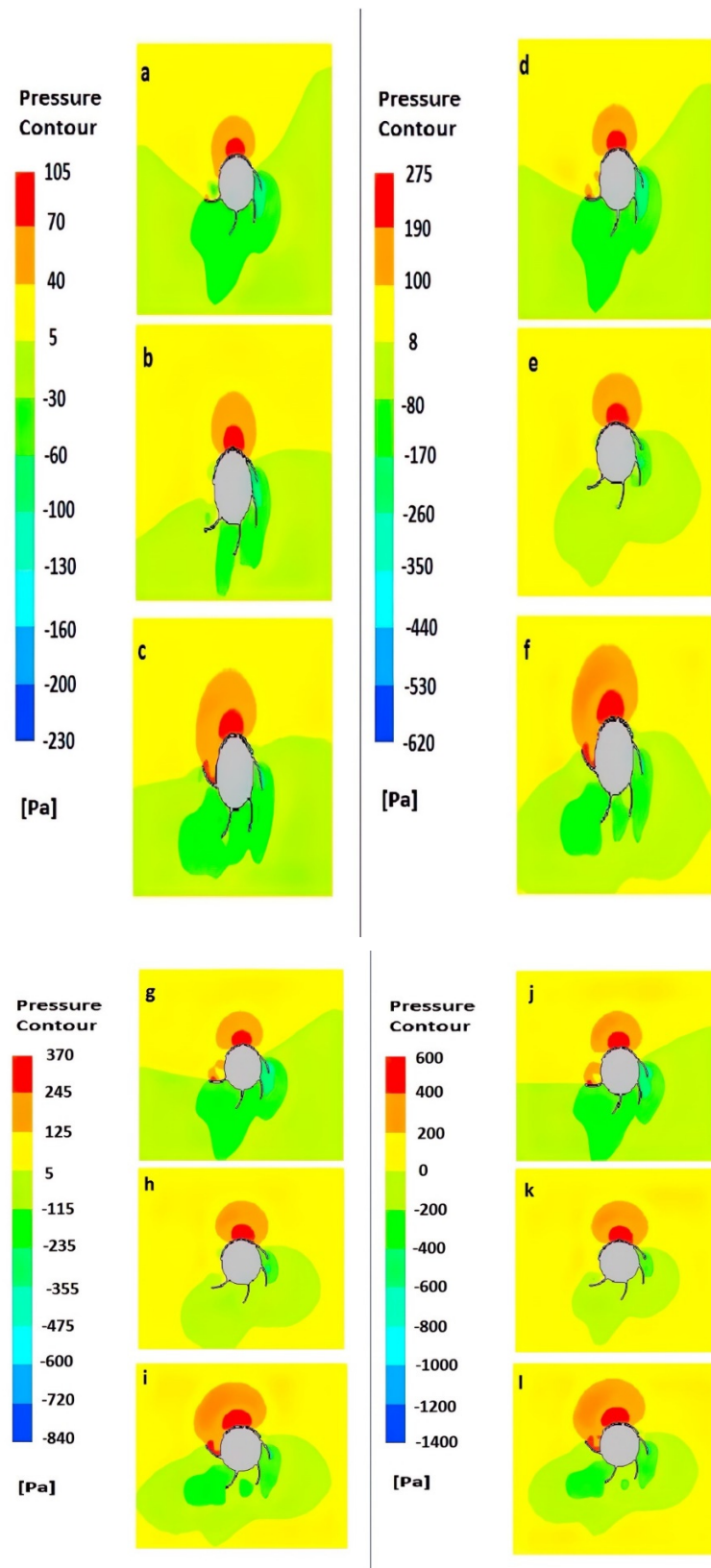
Figure 10. Pressure contours for 3D from θ = 0, 20, 50 and Cf 0.4 and 0.46. ((**a**): θ = 0, Cf = 0.4; (**b**): θ = 20, Cf = 0.4; (**c**): θ = 50, Cf = 0.4; (**d**): θ = 0, Cf = 0.46; (**e**): θ = 20, Cf = 0.46; (**f**): θ = 50, Cf = 0.46). θ = 0, 20, 50 and Cf 0.49 and 0.52. ((**g**): θ = 0, Cf = 0.49; (**h**): θ = 20, Cf = 0.49; (**i**): θ = 50, Cf = 0.49; (**j**): θ = 0, Cf = 0.52; (**k**): θ = 20, Cf = 0.52; (**l**): θ = 50, Cf = 0.52).
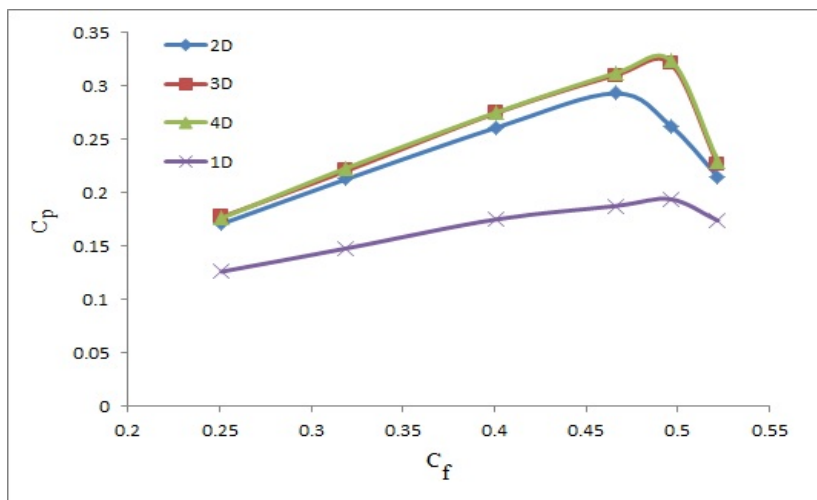
Figure 11. The turbine performances in different submerged depths.

Figure 11. illustrates the pressure contours of the turbine at different vertical positions, a rotation angle of 50, and a flow coefficient of 0.46. It is evident from the figure that as the height increases, the static pressure, total pressure, low-pressure area, and back pressure behind the turbine also increase due to the effect of static pressure. The pressure contours of the turbine in different vertical positions, with a rotation angle is shown in Figure 12.
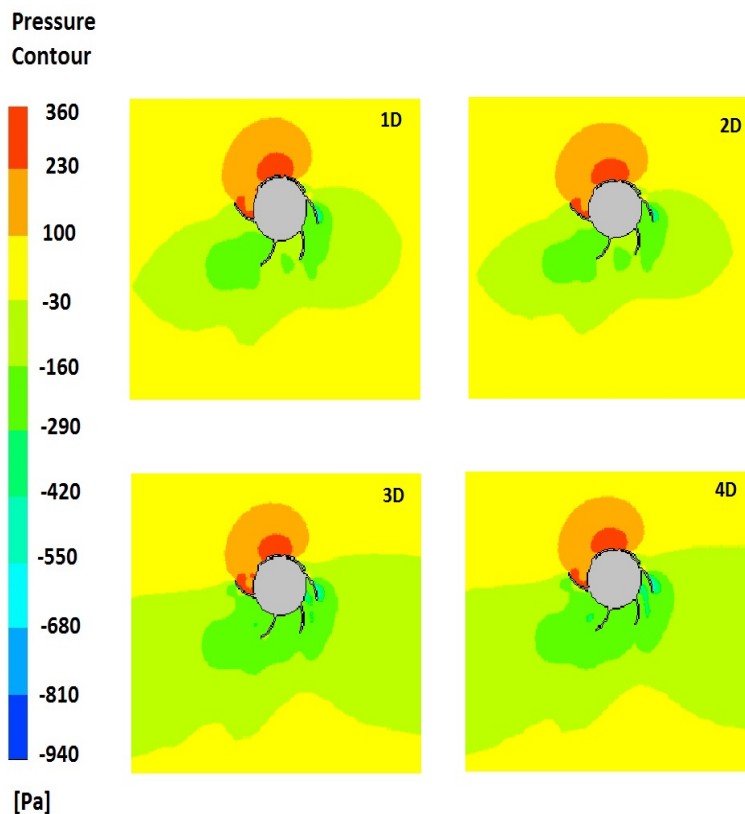

Figure 12. The pressure contours of the turbine in different vertical positions, with a rotation angle of 50 and a flow coefficient of 0.46.

In submerged depths of 2D and 3D, by increasing the flow coefficient from 0.25 to 0.52, the maximum torque produced by the turbine increases from 1.1 Nm to 2.1 Nm and from 1.3 Nm to 2.2 Nm, respectively. However, in depths of 4D and 5D, the maximum torque

produced by the turbine is relatively constant, ranging from 1.7 Nm to 1.9 Nm and from 1.9 Nm to 2 Nm, respectively, for flow coefficients ranging from 0.25 to 0.52.

It can be observed from Figures 13–16 that the maximum torque produced by the turbine occurs at a rotational angle of 10 degrees in all flow coefficients and submerged depths. At a rotational angle of 30 degrees, the torque produced by the turbine is minimum. Furthermore, the results show that the optimum submerged depth for the turbine is 3D, as it produces the highest torque in all flow coefficients. This result is consistent with the findings in the previous section, which showed that the best position for placing the turbine is at a depth of 3D.
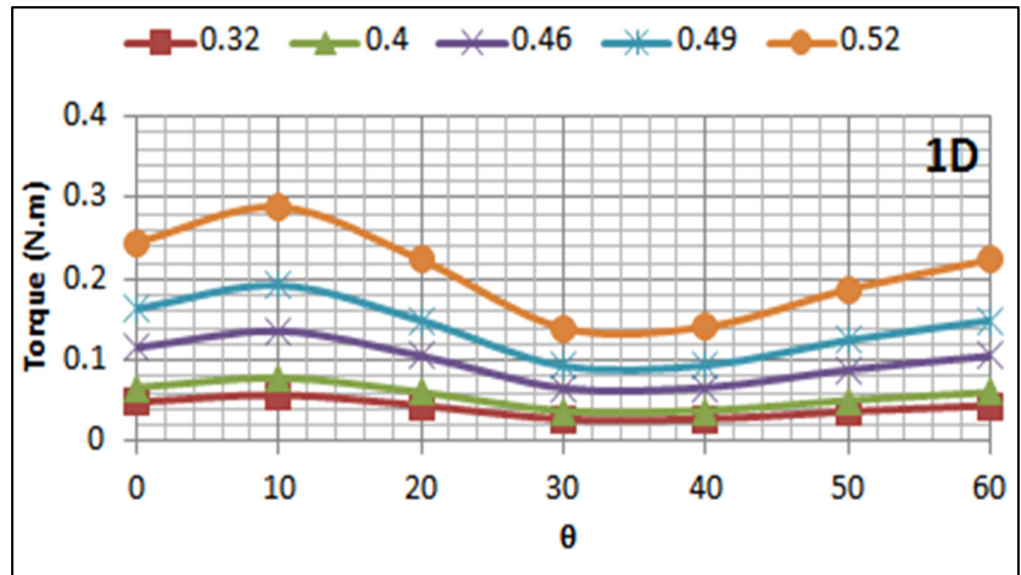

Figure 13. The trend of change of total torque with angle of rotation with various flow coefficients in 1D depth.
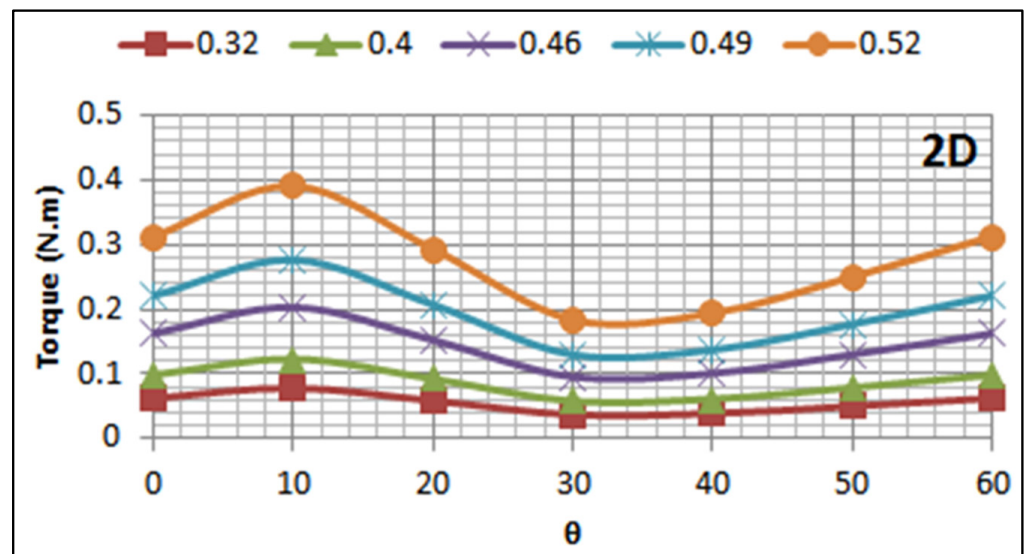

Figure 14. The trend of change of total torque with angle of rotation with various flow coefficients in 2D depth.
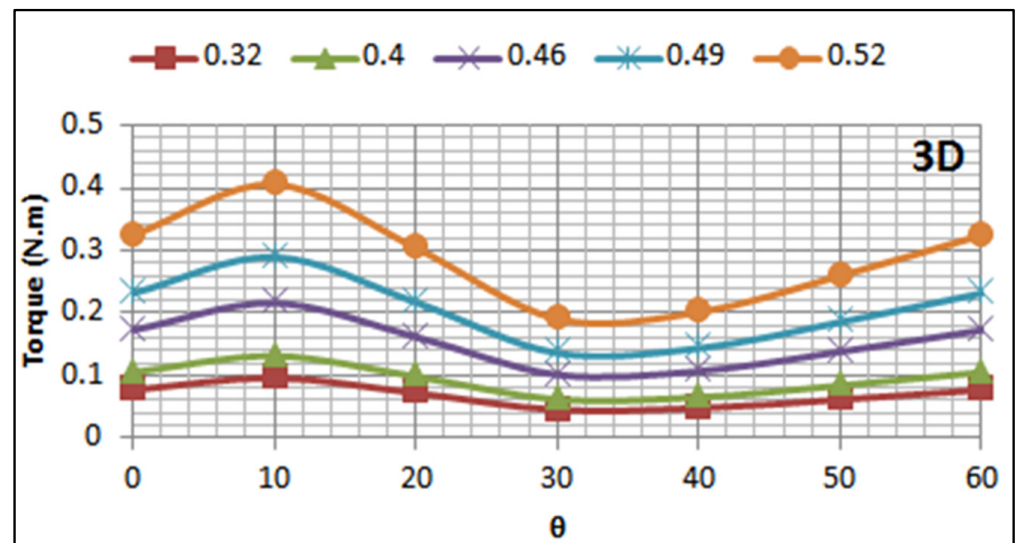
Figure 15. The trend of change of total torque with angle of rotation with various flow coefficients in 3D depth.
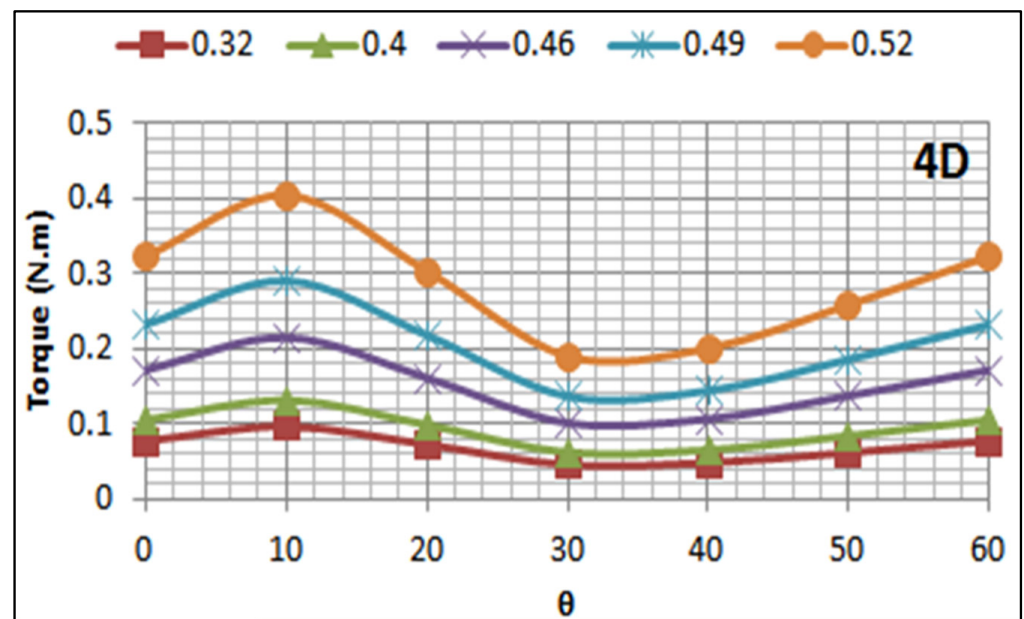

Figure 16. The trend of change of total torque with angle of rotation with various flow coefficients in 4D depth.

Figures 17–20 depict the turbine power coefficient in different submerged depths as a function of the rotational angle and flow coefficient. It is evident that the turbine power coefficient increases for all flow coefficients from $\theta = 0°$ to $\theta = 10°$ and reaches its maximum value, as the turbine generates the highest torque at $\theta = 10°$. Then, the trend changes, and the power coefficient decreases by increasing the rotational angle, reaching its minimum value at $\theta = 30°$. Subsequently, the turbine power coefficient increases again from $\theta = 30°$ to $\theta = 60°$. The flow coefficient of 0.32 results in the best turbine power coefficient, whereas the worst performance is observed in the flow coefficient of 0.52. Furthermore, the power coefficient initially increases with an increase in the submerged depth and becomes equal for depths of 3D and 4D.
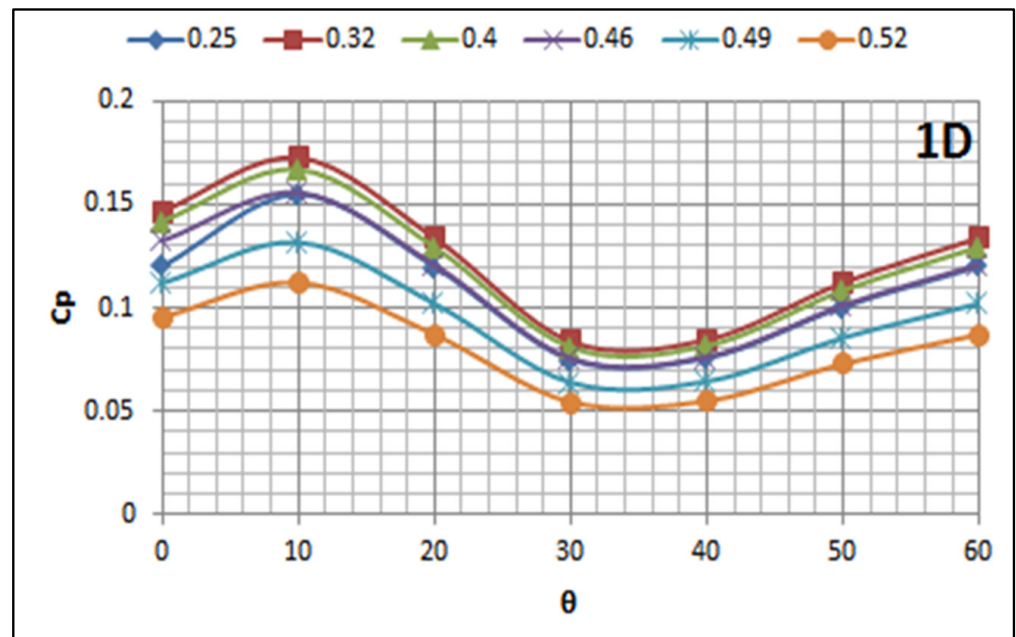
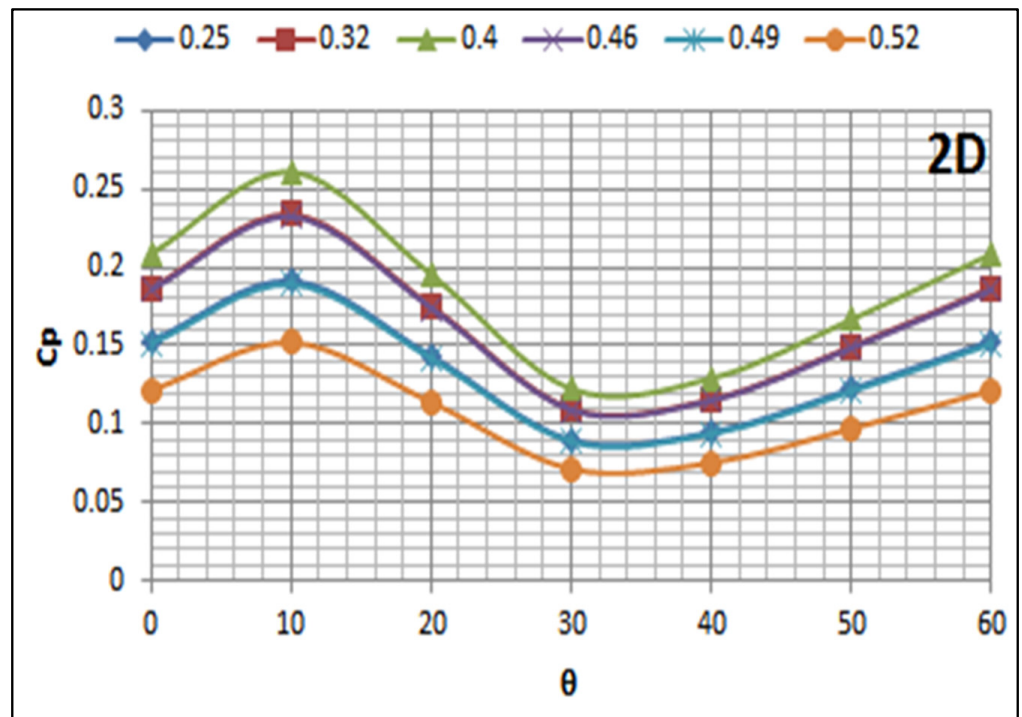**Figure 17.** The trend of change of power coefficient with angle of rotation with various flow coefficients in 1D depth.

Figure 18. The trend of change of power coefficient with angle of rotation with various flow coefficients in 2D depth.
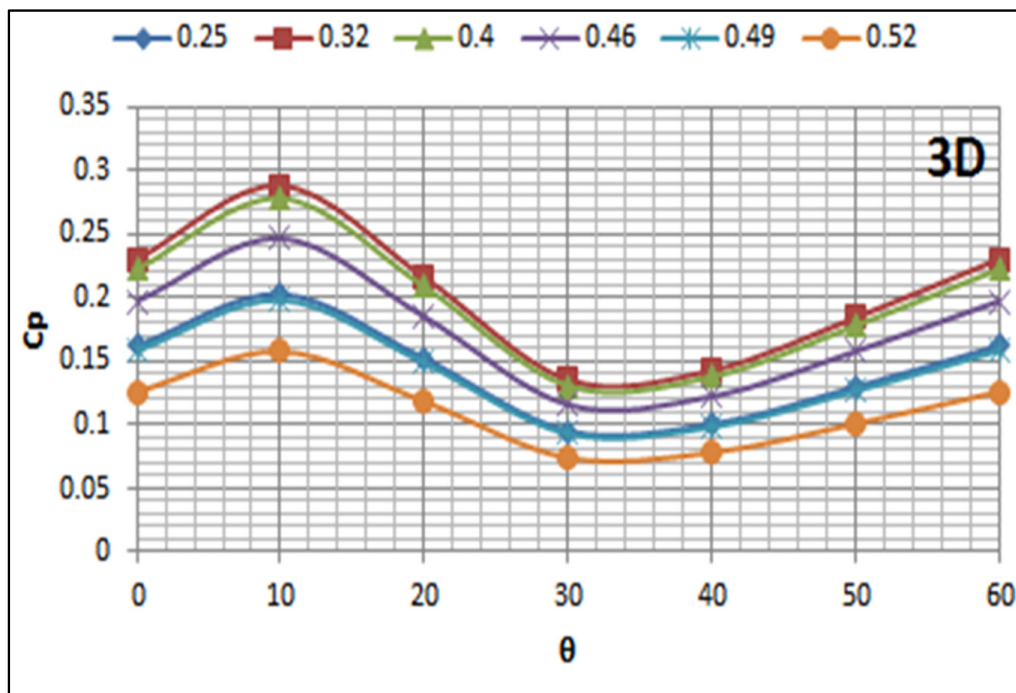
Figure 19. The trend of change of power coefficient with angle of rotation with various flow coefficients in 3D depth.
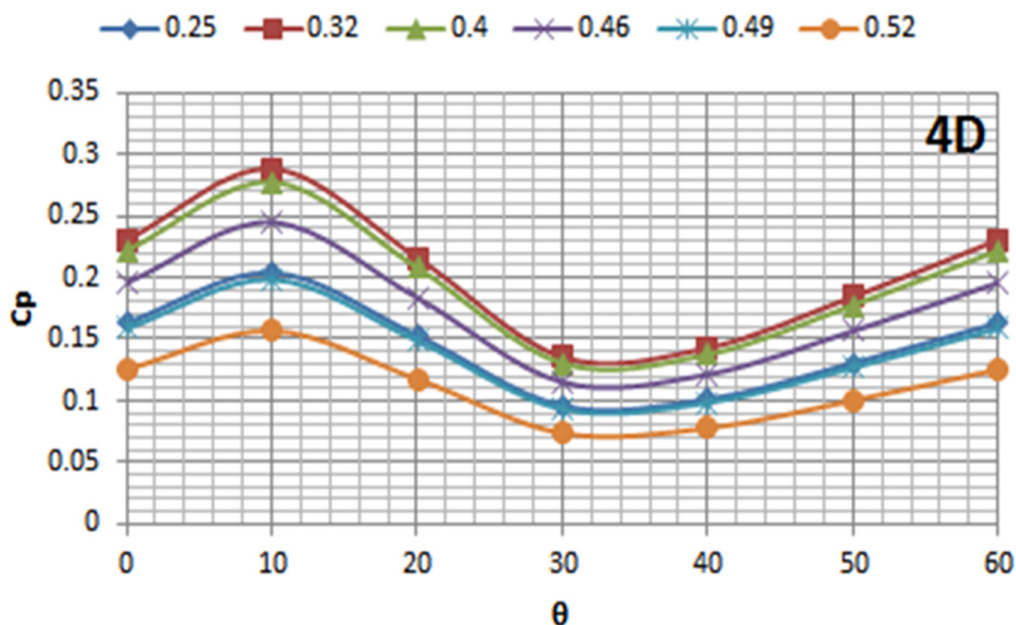

Figure 20. The trend of change of power coefficient with angle of rotation with various flow coefficients in 4D depth.

6. Conclusions

The present study aimed to analyze a vertical axis tidal turbine (VATT) both experimentally and numerically. Initially, an experimental model of the Hunter turbine was designed with an aspect ratio of 1.2 and tested in a water channel. Laboratory data were used to verify the RANS equations, which were implemented around the turbine using CFD software. The effect of the turbine's submerged depth from the water surface on its performance was then investigated. The turbine was analyzed at four different depths: 1D, 2D, 3D, and 4D. The numerical solution was reasonably close to the experimental data. The

results demonstrated that as the vertical distance from the water surface increased, the energy that could be harnessed from the water flow also increased, resulting in improved turbine performance. However, there was a specific height beyond which increasing the vertical distance did not enhance the turbine's performance. In other words, there was a minimum depth required for achieving maximum power output, which was found to be 3D. Moreover, this study revealed that the maximum power coefficient of the turbine was observed in smaller flow coefficients with increased depth. The highest power coefficient achieved was 0.218 at a flow coefficient of 0.49 for submerged depths of 3D and 4D.

Author Contributions: Conceptualization, E.G. and H.K.; methodology, E.G., H.K. and S.H.; software, E.G. and H.K.; validation, E.G. and H.K.; formal analysis, E.G., H.K. and S.H.; investigation, E.G., H.K. and S.H.; resources, E.G., H.K. and S.H.; data curation, E.G. and H.K.; writing—original draft preparation, E.G. and H.K.; writing—review and editing, E.G., H.K. and S.H.; visualization, E.G., H.K. and S.H.; supervision, S.H.; project administration, E.G., H.K. and S.H. All authors have read and agreed to the published version of the manuscript.

Data Availability Statement: All data used to support the findings of this study are included in the article.

Conflicts of Interest: The authors declare no conflict of interest.

References

1. Harries, T.; Kwan, A.; Brammer, J.; Falconer, R. Physical testing of performance characteristics of a novel drag-driven vertical axis tidal stream turbine; with comparisons to a conventional Savonius. *Int. J. Mar. Energy* **2016**, *14*, 215–228. [CrossRef]
2. Kariman, H.; Hoseinzadeh, S.; Heyns, S.; Sohani, A. Modeling and exergy analysis of domestic MED desalination with brine tank. *Desalin. Water Treat.* **2020**, *197*, 1–13. [CrossRef]
3. Mansour, A.E.; Pedersen, P.T.; Paik, J.K. Wave energy extraction using decommissioned ships. *Ships Offshore Struct.* **2013**, *8*, 504–516. [CrossRef]
4. Kariman, H.; Hoseinzadeh, S.; Heyns, P.S. Energetic and exergetic analysis of evaporation desalination system integrated with mechanical vapor recompression circulation. *Case Stud. Therm. Eng.* **2019**, *16*, 100548. [CrossRef]
5. Derakhshan, S.; Kasaeian, N. Optimization, Numerical, and Experimental Study of a Propeller Pump as Turbine. *J. Energy Resour. Technol.-Trans. Asme* **2014**, *136*, 012005. [CrossRef]
6. Kariman, H.; Hoseinzadeh, S.; Shirkhani, A.; Heyns, P.S.; Wannenburg, J. Energy and economic analysis of evaporative vacuum easy desalination system with brine tank. *J. Therm. Anal. Calorim.* **2020**, *140*, 1935–1944. [CrossRef]
7. Khan, M.J.; Bhuyan, G.; Iqbal, M.T.; Quaicoe, J.E. Hydrokinetic energy conversion systems and assessment of horizontal and vertical axis turbines for river and tidal applications: A technology status review. *Appl. Energy* **2009**, *86*, 1823–1835. [CrossRef]
8. Martin-Short, R.; Hill, J.; Kramer, S.C.; Avdis, A.; Allison, P.A.; Piggott, M.D. Tidal resource extraction in the Pentland Firth, UK: Potential impacts on flow regime and sediment transport in the Inner Sound of Stroma. *Renew. Energy* **2015**, *76*, 596–607. [CrossRef]
9. Sanchez, M.; Carballo, R.; Ramos, V.; Iglesias, G. Tidal stream energy impact on the transient and residual flow in an estuary: A 3D analysis. *Appl. Energy* **2014**, *116*, 167–177. [CrossRef]
10. Chen, L.; Lam, W.H. A review of survivability and remedial actions of tidal current turbines. *Renew. Sustain. Energy Rev.* **2015**, *43*, 891–900. [CrossRef]
11. Ma, Y.; Zhang, L.; Ma, L.; Chen, Z. Developing status and development trend of vertical axis turbine-type tidal current energy power generation device. *Keji Daobao Sci. Technol. Rev.* **2012**, *30*, 71–75.
12. Batten, W.M.J.; Bahaj, A.S.; Molland, A.F.; Chaplin, J.R. The prediction of the hydrodynamic performance of marine current turbines. *Renew. Energy* **2008**, *33*, 1085–1096. [CrossRef]
13. Li, Y.; Calisal, S.M. Numerical analysis of the characteristics of vertical axis tidal current turbines. *Renew. Energy* **2010**, *35*, 435–442. [CrossRef]
14. Copping, A.; Hanna, L.; Whiting, J.; Geerlofs, S.; Grear, M.; Blake, K.; Coffey, A.; Massaua, M.; Brown-Saracino, J.; Battey, H. *Environmental Effects of Marine Energy Development around the World*; Annex IV Final Report; IEA Ocean Energy Systems Initiative, Annex IV: Richland, WA, USA, 2013.
15. Jacobson, P.T.; Amaral, S.V.; Castro-Santos, T.; Giza, D.; Haro, A.J.; Hecker, G.; McMahon, B.; Perkins, N.; Pioppi, N. *Environmental Effects of Hydrokinetic Turbines on Fish: Desktop and Laboratory Flume Studies*; Electric Power Research Institute: Palo Alto, CA, USA, 2012.
16. Yang, B.; Lawn, C. Fluid dynamic performance of a vertical axis turbine for tidal currents. *Renew. Energy* **2011**, *36*, 3355–3366. [CrossRef]

17. Chen, B.; Cheng, S.B.; Su, T.C.; Zhang, H. Numerical investigation of channel effects on a vertical-axis tidal turbine rotating at variable speed. *Ocean Eng.* **2018**, *163*, 358–368. [CrossRef]

18. Jing, F.M.; Sheng, Q.H.; Zhang, L. Experimental research on tidal current vertical axis turbine with variable-pitch blades. *Ocean Eng.* **2014**, *88*, 228–241. [CrossRef]

19. Sun, J.J.; Huang, D.G. Numerical investigation on aerodynamic performance improvement of vertical-axis tidal turbine with super-hydrophobic surface. *Ocean Eng.* **2020**, *217*, 107995. [CrossRef]

20. Derakhshan, S.; Ashoori, M.; Salemi, A. Experimental and numerical study of a vertical axis tidal turbine performance. *Ocean Eng.* **2017**, *137*, 59–67. [CrossRef]

21. Maduka, M.; Li, C.W. Experimental evaluation of power performance and wake characteristics of twin flanged duct turbines in tandem under bi-directional tidal flows. *Renew. Energy* **2022**, *199*, 1543–1567. [CrossRef]

22. Arcos, F.Z.D.; Vogel, C.R.; Willden, R.H.J. A parametric study on the hydrodynamics of tidal turbine blade deformation. *J. Fluids Struct.* **2022**, *113*, 103626. [CrossRef]

23. Moreau, M.; Germain, G.; Maurice, G.; Richard, A. Sea states influence on the behaviour of a bottom mounted full-scale twin vertical axis tidal turbine. *Ocean Eng.* **2022**, *265*, 112582. [CrossRef]

24. Sun, K.; Yi, Y.; Zhang, J.S.; Zhang, J.H.; Zaidi, S.S.H.; Sun, S.H. Influence of blade numbers on start-up performance of vertical axis tidal current turbines. *Ocean Eng.* **2022**, *243*, 110314. [CrossRef]

25. Ma, Y.; Hu, C.; Li, L. Hydrodynamics and wake flow analysis of a Π-type vertical axis twin-rotor tidal current turbine in surge motion. *Ocean Eng.* **2021**, *224*, 108625. [CrossRef]

26. Satrio, D.; Utama, I.K.A.P. Experimental investigation into the improvement of self-starting capability of vertical-axis tidal current turbine. *Energy Rep.* **2021**, *7*, 4587–4594. [CrossRef]

27. Chen, Y.L.; Sun, J.; Lin, B.L.; Lin, J.; Guo, J.X. Spatial evolution and kinetic energy restoration in the wake zone behind a tidal turbine: An experimental study. *Ocean Eng.* **2021**, *228*, 108920. [CrossRef]

28. Xie, J.M.; Chen, J.Y. Vertical-axis ocean current turbine design research based on separate design concept. *Ocean Eng.* **2019**, *188*, 106258. [CrossRef]

29. Han, J.; Jung, J.; Hwang, J.H. Optimal configuration of a tidal current turbine farm in a shallow channel. *Ocean Eng.* **2021**, *220*, 108395. [CrossRef]

30. Manolesos, M.; Chng, L.; Kaufmann, N.; Ouro, P.; Ntouras, D.; Papadakis, G. Using vortex generators for flow separation control on tidal turbine profiles and blades. *Renew. Energy* **2023**, *205*, 1025–1039. [CrossRef]

31. Wang, P.Z.; Zhao, B.W.; Cheng, H.T.; Huang, B.; He, W.S.; Zhang, Q.; Zhu, F.W. Study on the performance of a 300W counter-rotating type horizontal axis tidal turbine. *Ocean Eng.* **2022**, *255*, 111446. [CrossRef]

32. Samadi, M.; Hassanabad, M.G.; Mozafari, S.B. Performance enhancement of low speed current savonius tidal turbines through adding semi-cylindrical deflectors. *Ocean Eng.* **2022**, *259*, 111873. [CrossRef]

33. Khanjanpour, M.H.; Javadi, A.A. Optimization of a Horizontal Axis Tidal (HAT) turbine for powering a Reverse Osmosis (RO) desalination system using Computational Fluid Dynamics (CFD) and Taguchi method. *Energy Convers. Manag.* **2021**, *231*, 113833. [CrossRef]

34. Yang, B.; Lawn, C. Three-dimensional effects on the performance of a vertical axis tidal turbine. *Ocean Eng.* **2013**, *58*, 1–10. [CrossRef]

35. Wang, X.L.; Qiao, D.S.; Jin, L.X.; Yan, J.; Wang, B.; Li, B.B.; Ou, J.P. Numerical investigation of wave run-up and load on heaving cylinder subjected to regular waves. *Ocean Eng.* **2023**, *268*, 113415. [CrossRef]

36. Liang, H.Z.; Qiao, D.S.; Wang, X.Z.; Zhi, G.N.; Yan, J.; Ning, D.Z.; Ou, J.P. Energy capture optimization of heave oscillating buoy wave energy converter based on model predictive control. *Ocean Eng.* **2023**, *268*, 113402. [CrossRef]

37. Wang, Z.M.; Qiao, D.S.; Yan, J.; Tang, G.Q.; Li, B.B.; Ning, D.Z. A new approach to predict dynamic mooring tension using LSTM neural network based on responses of floating structure. *Ocean Eng.* **2022**, *249*, 110905. [CrossRef]

38. Nazarieh, M.; Kariman, H.; Hoseinzadeh, S. Numerical simulation of fluid dynamic performance of turbulent flow over Hunter turbine with variable angle of blades. *Int. J. Numer. Methods Heat Fluid Flow* **2023**, *33*, 153–173. [CrossRef]